Plasmon–Enhanced Energy Transfer for Improved Upconversion of Infrared Radiation in Doped-Lanthanide Nanocrystals

6 AUTHORS, INCLUDING:

Q. -C. Sun
University of Colorado Boulder
35 PUBLICATIONS   231 CITATIONS

SEE PROFILE

Haridas Mundoor
University of Colorado Boulder
20 PUBLICATIONS   153 CITATIONS

SEE PROFILE

Ivan I Smalyukh
University of Colorado Boulder
160 PUBLICATIONS   3,025 CITATIONS

SEE PROFILE

# Plasmon-Enhanced Energy Transfer for Improved Upconversion of Infrared Radiation in Doped-Lanthanide Nanocrystals

Qi-C. Sun,[†] Haridas Mundoor,[‡] Josep C. Ribot,[†] Vivek Singh,[†] Ivan I. Smalyukh,[‡,§,‖] and Prashant Nagpal*[,†,§,‖]

[†]Department of Chemical and Biological Engineering, [‡]Department of Physics, [§]Materials Science and Engineering, and [‖]Renewable and Sustainable Energy Institute (RASEI), University of Colorado Boulder, Boulder, Colorado 80309, United States

S Supporting Information

ABSTRACT: Upconversion of infrared radiation into visible light has been investigated for applications in photovoltaics and biological imaging. However, low conversion efficiency due to small absorption cross-section for infrared light (Yb^{3+}), and slow rate of energy transfer (to Er^{3+} states) has prevented application of upconversion photoluminescence (UPL) for diffuse sunlight or imaging tissue samples. Here, we utilize resonant surface plasmon polaritons (SPP) waves to enhance UPL in doped-lanthanide nanocrystals. Our analysis indicates that SPP waves not only enhance the electromagnetic field, and hence weak Purcell effect, but also increase the rate of resonant energy transfer from Yb^{3+} to Er^{3+} ions by 6 fold. While we do observe strong metal mediated quenching (14-fold) of green fluorescence on flat metal surfaces, the nanostructured metal is resonant in the infrared and hence enhances the nanocrystal UPL. This strong Coulombic effect on energy transfer can have important implications for other fluorescent and excitonic systems too.

KEYWORDS: Upconversion, surface plasmon, energy transfer, nanoparticles, photophysics
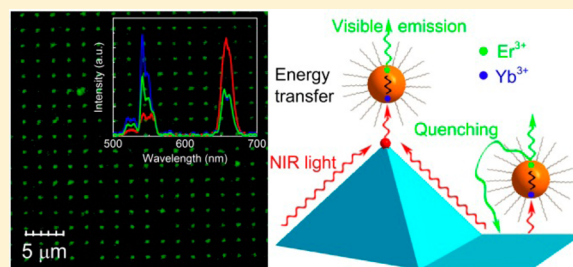
Incident solar radiation is energetically broad and poses challenges for efficient conversion to electricity using a finite bandgap semiconductor photocell.[1,2] Even with optimized silicon semiconductor, 30% of the incident radiation is not absorbed and is simply transmitted through (Figure 1a, green shaded region). Considering a thermodynamic maximum conversion efficiency limit of 31% sunlight into electricity,[3] this unused infrared radiation provides an important opportunity for enhancing the current efficiency of solar cell for renewable energy generation. Although the infrared photons have insufficient energy, combining two or more infrared photons to generate a single visible or ultraviolet photon, a process known as upconversion, can have important implications for solar energy conversion.[4,5] Similar upconversion can benefit existing biological imaging techniques, because while most photodetectors are efficient in visible wavelengths, biological tissue and samples (like melanin, water, hemoglobin, and so forth,[6] Figure 1b) have a narrow window of optical transparency for infrared photons. While this allows infrared wavelengths to penetrate deep in tissue and allow facile optical imaging, the light needs to be upconverted for easy detection by inexpensive photodetectors.[7−9] To design appropriate energy upconversion nanocrystals, we indicated the infrared radiation absorbed by respective lanthanide ions (in red symbols), and their counterpart upconverted radiation wavelengths (in green symbols) in Figure 1a. Although this provides an important opportunity for utilizing upconversion for renewable energy applications and biological imaging, some

physical processes limit the conversion efficiency and hence applicability of photoluminescence upconversion process (UPL).

UPL in doped lanthanide (Yb/Er codoped $NaYF_4$ here) nanocrystals is mediated by absorption of infrared light in dominant ytterbium ions (Yb^{3+}, 17%), followed by energy transfer to multiple energy states observed in minority Erbium dopant (Er^{3+}, 3%, Figure 1c), and radiative relaxation leading to emission of upconverted visible or ultraviolet light.[8,10−12] While UPL can also be accomplished by multiphoton absorption directly in Er^{3+} and Tm^{3+} ions (Figure 1a), this process served as a model system to study important physical processes like enhancing small absorption cross-section in doped ions, energy transfer, multiple relaxation (radiative and phonon relaxation) pathways to understand fundamental photophysics in these photoexcited states. Moreover, fast phonon cooling to ground state, low absorption cross-section (especially for multi-photons), and multiple nonradiative relaxation pathways (Figure 1c) lead us to choose Yb^{3+} ions as infrared absorbers, and Er^{3+} ions as UPL emitter in this study.

We excited the β-$NaYF_4$:17%Yb^{3+}/3%Er^{3+} upconverting nanoparticles (UCNP Figure 2a, see Methods) in films on glass and gold substrates, using 980 nm infrared diode laser, and monitored the upconverted red and green light as a
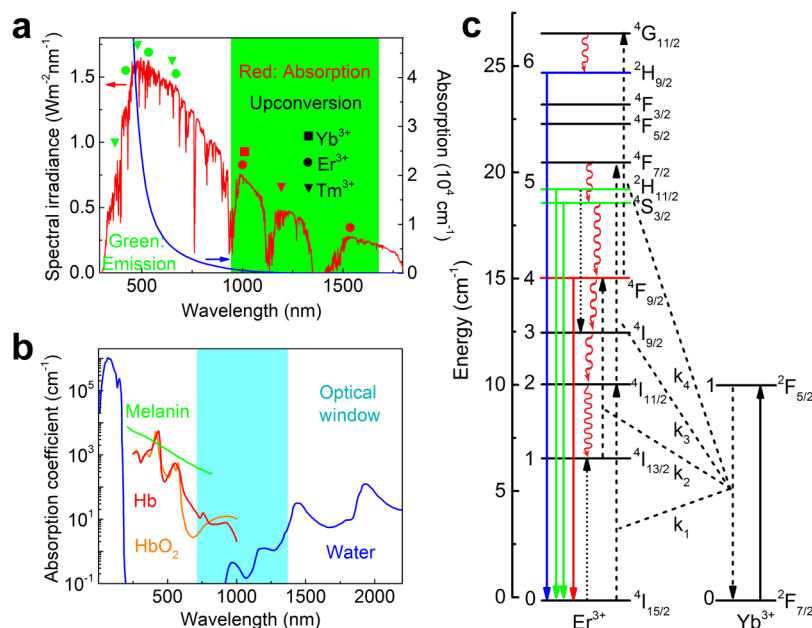
Figure 1. Upconversion in doped lanthanides for solar energy and bioimaging. (a) AM 1.5 incident solar radiation spectrum (red curve) and absorption of silicon (blue curve). More than a third of the incident solar radiation is simply transmitted through a silicon photocell. Green circles and triangles show the visible upconverted emission of Er^{3+} and Tm^{3+}, whereas red circles, triangle, and square indicate the infrared absorption of Er^{3+}, Tm^{3+}, and Yb^{3+}, respectively. The green shaded region indicates the upconversion region, where the doped lanthanide ions (Yb^{3+}, Er^{3+} and Tm^{3+}) absorb the infrared radiation. (b) The absorption spectrum of major tissue light absorbers hemoglobin, melanin, and water.[6] This "optical window" of biological transparency, between 800 and 1300 nm, allows biological tissues to be imaged easily using infrared radiation. This window overlaps well with the upconversion absorbers, which can convert the incident infrared light to visible radiation, for facile detection by current optical detectors for bioimaging applications. (c) Energy-level diagram, upconversion excitation, and visible emission schemes for the Yb^{3+}-sensitized Er^{3+} system.[10,12] Dashed, solid, curly, and dotted arrows indicate upconversion energy transfer, radiative, multiphonon, and cross-relaxation processes, respectively. The high efficiency in the upconversion processes can be achieved by improving the absorption in Yb^{3+} dopants and enhancing the energy transfer between Er^{3+} and Yb^{3+} (dashed lines). Yb^{3+} mainly absorbs 980 nm photons.
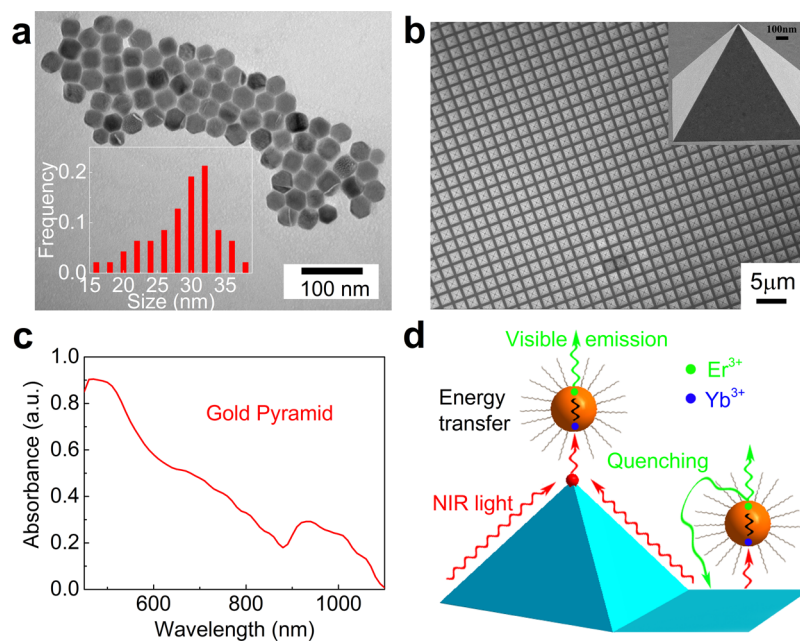

Figure 2. Tuning the resonant plasmon of nanostructured metal in the infrared. (a) A representative TEM image of 29 nm β-NaYF$_4$:17%Yb^{3+}/3% Er^{3+} nanoparticles. The inset shows the size distribution obtained from several TEM images. (b) Scanning electron micrograph of a gold pyramid array, made by optical lithography and anisotropic KOH etching, with 2 μm periodicity. The inset shows higher resolution image of the gold pyramid at a steep angle. (c) Optical absorbance spectrum of the gold pyramid substrate. There is a clear broad plasmon absorption peak at ~980 nm. The peak ~500 nm is attributed to interband d-transitions in gold metal. (d) Schematic of the energy transfer, upconversion, and quenching processes on the top and bottom of the gold pyramid substrate. The ultrasmooth gold pyramid provides a good platform to study all of these photophysical processes in the doped-lanthanide nanoparticles.
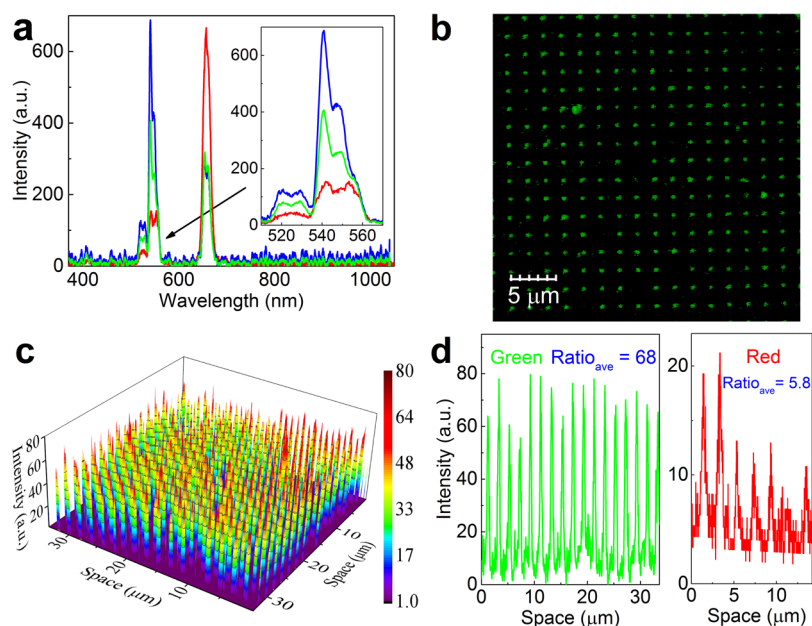
Figure 3. Plasmon enhanced upconversion in Yb^{3+}/Er^{3+} doped lanthanide nanoparticles. (a) Upconversion emission spectra of 29 nm β-NaYF$_4$:17% Yb^{3+}/3%Er^{3+} nanoparticles on the gold pyramid (red curve), flat gold (green curve), and glass substrate (blue curve), respectively. (b) Confocal images for the green emission on 29 nm NaYF$_4$:Yb^{3+}/Er^{3+} particles. (c) Three-dimensional confocal scan images of the green emission on 29 nm NaYF$_4$:Yb^{3+}/Er^{3+} particles. (d) Spatially resolved line intensity for the green and red upconversion emission on the gold pyramid, using the 3D image. The confocal scans clearly show high enhancement in upconversion photoluminescence, especially at the gold pyramid tip. For green UPL, strong quenching can also be observed on the flat gold metal.

function of time. We observed single exponential decay dynamics (Supporting Information Figure S1) for both red and green upconverted light. This indicates that the non-radiative relaxation pathways are likely less dominant in these synthesized UCNP's (Figure 1c). Also, the long lifetimes of the upconverted radiation (Supporting Information Figure S1, also reported by other groups)[13−16] indicates that it is possible to utilize incident (or concentrated) solar radiation for upconversion of infrared photons (Figure 1a, Supporting Information Figure S2 discussion). While high laser intensities can be used for single nanoparticle imaging,[17] intense infrared radiation can cause photodamage to tissues. Therefore, the poor conversion efficiency of as-synthesized UCNP's can limit their applications for renewable energy (too high concentration of sunlight required) or biological applications. The physical processes limiting the upconversion process in these nanoparticles have been identified as weak absorption in Yb^{3+} and low rate of energy transfer to Er^{3+} (see detailed analysis in Supporting Information). We improved the absorption of infrared radiation (in Yb^{3+}) using electromagnetic or Purcell enhancement[18−20] and enhanced the energy transfer rates to minority Erbium dopant, using coupled light-electron waves, or surface plasmon polaritons, on nanopatterned metal surfaces.

Surface plasmon polaritons are surface waves that can produce large fluctuations of charges (and electric field), resonant with the incident light waves.[18−25] These massive charge fluctuations have been theorized to have a strong Coulombic effect on the near-field electronic phenomenon.[26] We used these SPP waves to enhance the local electric field and hence the weak absorption in doped Yb^{3+} ions. Possible coupling of energy transfer process with the charge fluctuation can also result in an increase of UPL process and can be decoupled from the Purcell or electromagnetic field enhancement by detailed analysis of ensuing photophysics. To study

these effects, we started with a patterned gold pyramid substrate, fabricated by template stripping process (Figure 2b).[20,24] The template stripping process defined very uniform electric field enhanced spots at the tip, with the field enhancement ∼5 at the apex for patterned gold pyramids.[20] We synthesized β-NaYF$_4$:17%Yb^{3+}/3%Er^{3+} nanoparticles (see Methods, transmission electron micrograph (TEM) in Figure 2a) and uniformly coated the gold pyramid substrate with nanoparticles (see Methods and Supporting Information Figure S3). Because the Yb^{3+} absorption occurs at ∼980 nm,[10,13,15] the absorbance of the designed gold pyramid pattern was tuned with an SPP mode around 980 nm (Figure 2c and Supporting Information Figure S4, 2 μm periodicity).

Coupling between phosphors and metallic surface or nanoparticles is a well-known method to enhance fluorescence.[19,27] It is well understood that the local electric field distribution is altered as the phosphor approaches the metal nanostructure. Thus, metal surfaces and nanoparticles can result in enhancement or quenching of fluorescence depending on the distance and geometry.[27] While the electric field enhancement near a patterned metal surface can enhance both excitation and emission rate of phosphors (or quenching leading to reduction of steady state PL), in UCNP's the absorption enhancement is accompanied by transfer of energy to Er^{3+} energy levels (Figure 1c). Therefore, electromagnetic field or Purcell enhancement of absorption (Yb^{3+}), quenching, and energy transfer needs to be decoupled to understand the photophysics of UPL on nanopatterned metal surfaces (Figure 2d). We developed a model describing photoexcitation, energy transfer, occupation of different Er^{3+} energy levels, and radiative and nonradiative recombination[10,15] (see detailed model in Supporting Information). We also conducted experimental measurements to understand relative importance of the photophysical processes. The model is described briefly in

the following (see detailed model in Supporting Information, Figure 1c)

$$\frac{dN_{Er,1}}{dt} = W_{21}N_{Er,2} + C_{50}N_{Er,5}N_{Er,0} - \sigma_{14}IN_{Er,1} - k_2N_{Er,1}N_{Yb,1} - W_1N_{Er,1}$$

$$\frac{dN_{Er,2}}{dt} = W_{32}N_{Er,3} + \sigma_{02}IN_{Er,0} + k_1N_{Er,0}N_{Yb,1} - \sigma_{25}IN_{Er,2} - k_3N_{Er,2}N_{Yb,1}$$
$$- W_2N_{Er,2} - W_{21}N_{Er,2}$$

$$\frac{dN_{Er,3}}{dt} = W_{43}N_{Er,4} + C_{50}N_{Er,5}N_{Er,0} - W_{32}N_{Er,3} - W_3N_{Er,3}$$

$$\frac{dN_{Er,4}}{dt} = \sigma_{14}IN_{Er,1} + k_2N_{Er,1}N_{Yb,1} + W_{54}N_{Er,5} - \sigma_{46}IN_{Er,4} - k_4N_{Er,4}N_{Yb,1}$$
$$- W_{43}N_{Er,4} - W_4N_{Er,4}$$

$$\frac{dN_{Er,5}}{dt} = \sigma_{25}IN_{Er,2} + k_3N_{Er,2}N_{Yb,1} + W_{65}N_{Er,6} - C_{50}N_{Er,5}N_{Er,0} - W_{54}N_{Er,5}$$
$$- W_5N_{Er,5}$$

$$\frac{dN_{Er,6}}{dt} = \sigma_{46}IN_{Er,4} + k_4N_{Er,4}N_{Yb,1} - W_6N_{Er,6} - W_{65}N_{Er,6}$$

$$\frac{dN_{Yb,1}}{dt} = I\sigma_{Yb}N_{Yb,0} - k_1N_{Er,0}N_{Yb,1} - k_2N_{Er,1}N_{Yb,1} - k_3N_{Er,2}N_{Yb,1}$$
$$- k_4N_{Er,4}N_{Yb,1} - W_{Yb,1}N_{Yb,1}$$

where k is the energy transfer coefficient, N_i is the electron population of level i of Er^{3+} or Yb^{3+}, W_{ij} indicates the nonradiative relaxation rate from level i to level j of Er^{3+}, W_i is the radiative decay rate of level i of Er^{3+}, $W_{Yb,1}$ is the radiative decay rate of level 1 of Yb^{3+}, C_{50} is the rate of reverse-Auger like cross relaxation for $^2H_{11/2} + {}^4I_{15/2} \rightarrow {}^4I_{13/2} + {}^4I_{9/2}$ (Figure 1c).[28] σ_{ij} is the absorption cross section between level i and j of Er^{3+}, σ_{Yb} is the absorption cross section between level 0 and 1 of Yb^{3+}, and I is the pump flux. We conducted detailed experiments to refine the model. For example, we measured the absorbance of nanoparticles, and absence of direct absorption by the minority Er^{3+} dopants and low Er^{3+} doping level (with low absorption cross-section[29]) led us to neglect the direct single ($W_1N_{Er,1}$) and two- or three-photon absorption ($\sigma_{25}IN_{Er,2}$, $\sigma_{14}IN_{Er,1}$, $\sigma_{46}IN_{Er,4}$), especially compared to the low absorption in minority Er^{3+} ions and plasmon enhanced energy transfer rates from Yb^{3+} in these experiments. Moreover, direct measurements of UPL (Figure 3a) on glass substrate reveals that direct emission from level 3 ($W_3N_{Er,3}$, Figure 1c) is not observed, and hence reverse Auger-like cross-relaxation process ($C_{50}N_{Er,5}N_{Er,0}$, shown with dotted arrows, Figure 1c) and also the occupation of this intermediate level is negligible at steady state. Further, the single exponential decay dynamics shown in time-resolved PL (Supporting Information Figure S1) for both red and green emission indicates the nonradiative relaxation processes for levels 4 and 5 ($W_{54}N_{Er,5}$, $W_{43}N_{Er,4}$) can be neglected when compared to other energy transfer and radiative relaxation ($k_2N_{Er,1}N_{Yb,1}$, $W_4N_{Er,4}$ and $k_3N_{Er,2}N_{Yb,1}$, $W_5N_{Er,5}$). Therefore, at steady state, we can simplify the model as

$$0 = W_{21}N_{Er,2} - k_2N_{Er,1}N_{Yb,1} \tag{1}$$

$$0 = k_1N_{Er,0}N_{Yb,1} - k_3N_{Er,2}N_{Yb,1} - W_{21}N_{Er,2} \tag{2}$$

$$0 = k_2N_{Er,1}N_{Yb,1} - W_4N_{Er,4} \tag{3}$$

$$0 = k_3N_{Er,2}N_{Yb,1} - W_5N_{Er,5} \tag{4}$$

$$0 = fI\sigma_{Yb}N_{Yb,0} - k_1N_{Er,0}N_{Yb,1} - k_2N_{Er,1}N_{Yb,1} - k_3N_{Er,2}N_{Yb,1} \tag{5}$$

where, fI is the fraction of photoexcited Yb^{3+} that transfer their energy to Er^{3+} (excluding radiative relaxation of Yb, which is proportional to photoexcitation rate). This simplified model and experiments reveal several important insights into the photophysics of this coupled system. The relative distinct green emitting states ($^2H_{11/2}$, $^4S_{3/2}$, as shown in Figures 1c and inset of Figure 3a), reveals the relative occupation of these states and importance of cooling rates. We also used the ratio of red to green emission ($R_{G/R} = (W_5N_{Er,5})/(W_4N_{Er,4}) = (k_3/W_{21})(fI\sigma_{Yb}N_{Yb})/(2k_1N_{Er})$, using eqs 1, 2, 4, and 5, see Supporting Information for details) and the linear dependence on excitation rate (Supporting Information Figure S2) to account for enhanced phonon cooling (from level 2 to1) due to Purcell enhancement $W_{21}(T) = W_{21}(0)\{1/(\exp[(\hbar\omega)/(k_BT)] - 1) + 1\}^p$,[30] where, k_B is the Boltzmann constant, T is temperature, and p is the number of phonons, see Supporting Information) in plasmon enhanced UPL.

We used a gold pyramid pattern (Figure 2b) with 2 μm periodicity, fabricated using template stripping process (see Methods[24]). The ultrasmooth surfaces were used with well-defined plasmon hot-spots (no roughness for local enhancement[20]) at the gold pyramid tip (Figure 3b,c), combined with the flat gold surfaces, to investigate the Purcell enhancement, quenching, phonon relaxation, and energy transfer. We used spectrally resolved multiphoton confocal measurements (Figures 3b−d and 4a, Supporting Information Figure S6),
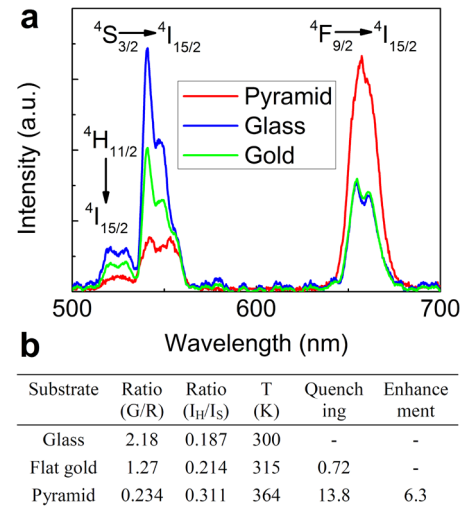

a

$^4S_{3/2} \rightarrow {}^4I_{15/2}$ $^4F_{9/2} \rightarrow {}^4I_{15/2}$

$^4H_{11/2}$ $^4I_{15/2}$

Intensity (a.u.)

— Pyramid
— Glass
— Gold

500 600 700
Wavelength (nm)

b

Substrate	Ratio (G/R)	Ratio (I_H/I_S)	T (K)	Quenching	Enhancement
Glass	2.18	0.187	300	-	-
Flat gold	1.27	0.214	315	0.72	-
Pyramid	0.234	0.311	364	13.8	6.3

Figure 4. Analysis of energy transfer enhancement and quenching due to plasmons. (a) UPL spectrum for the green and red upconversion observed from 29 nm $NaYF_4:Yb^{3+}/Er^{3+}$ particles on glass, gold, and gold pyramid substrates, respectively. (b) Summary of the upconversion emission intensity ratio of the green to red (G/R), UPL emission from $^2H_{11/2}$ to $^4S_{3/2}$ level (I_H/I_S), the temperature estimates for the substrates using the ratio of $^2H_{11/2}$ to $^4S_{3/2}$ level (for phonon assisted cooling in Er^{3+}), quenching, and energy transfer enhancement (see Supporting Information for detailed analysis).

combined with our model, to decouple these photophysical effects. Using previous investigation into 3D plasmonic nanofocusing,[20] we found the electromagnetic enhancement at the tip of patterned gold pyramid ∼5 times (although well designed patterned gold pyramids can achieve 80−100 fold enhancement). Using this experimental data, along with

estimates of temperature (Figure 4b, see details in Supporting Information) determined from the ratio of red to green emission (Figure 4a) for glass, flat gold, and patterned gold pyramids, we saw that green emission was strongly quenched on flat gold, whereas red UPL light was relatively unaffected. To account for this morphology dependent quenching, we modified eq 4 to include quenching for flat gold

$$0 = k_3 N_{Er,2} N_{Yb,1} - W_5 N_{Er,5} - k_q N_{Er,5} \qquad (6)$$

This dependence of quenching on gold metal is not surprising, since generation of propagating SPP waves can lead to strong quenching close to SPP wavelength (above SPP, additional momentum is required that is not present on ultrasmooth gold[24]). The absorption of gold pyramids clearly indicates that the tip SPP plasmon modes can only be excited close to 980 nm (Figure 2c). Therefore, while appreciable quenching is not observed for red emission (Figure 3d, Supporting Information Figure S6), the green emission is quenched on flat surfaces (Figure 3b,c), leading to large enhanced ratio (∼68 enhancement on tip compared to flat gold) and inverted ratios of green to red emission (Figure 4b, 2.2 to 0.2). Therefore, we can successfully decouple the effects of increased quenching (k_q enhanced ∼13.8 times, see Supporting Information), electromagnetic enhancement, and increased phonon cooling due to generation of plasmon waves.

To understand the effect of generation of SPP waves on energy transfer rates (from Yb^{3+} to Er^{3+}), we analyzed the experimental results for red UPL. After accounting for electromagnetic enhancements, and the effect on phonon cooling from level 2 to 1 (Figure 1c, $W_{21} = [k_3/(R_{G/R})][(fI\sigma_{Yb}N_{Yb})/(2k_1N_{Er})]$), we used the average enhancement of red emission due to plasmon-mediated energy transfer (comparing tip to bottom of gold pyramid, Figure 3d). We obtained an underestimate of the rate of energy transfer enhancement at 980 nm (plasmon enhanced ET) as 6.3 times (Figure 4b, see detailed analysis in Supporting Information). While the rate of energy transfer resonant with the plasmons at 980 nm (k_1) was enhanced 6.3 times, our analysis suggests that the other nonresonant energy transfer processes (k_2, k_3, and so forth) likely remain unchanged (or counterbalanced by enhanced phonon cooling, quenching). Therefore, this resonant energy transfer from Yb^{3+} to Er^{3+} ions is enhanced at least 6.3 times, thereby decoupling different photophysical effects in this model UPL system.

In order to investigate the effect of different plasmonic substrates for solar energy applications (Figure 1a), we also conducted depth-resolved imaging and UPL measurements on the bullseye and linear grating substrates, as shown in Supporting Information Figure S7–S9 (periodicity of the pattern was chosen based on measurements shown in Supporting Information Figure S4). Using the same analysis the enhancement and quenching for the substrates were decoupled, as shown in Supporting Information Table S1. The energy transfer enhancement obtained for both bullseye and linear grating (3.4 and 3.2, respectively) was lower than the pyramid substrate (6.3) with strong quenching effect observed on the flat gold, compared with the patterned metal resonant in the near-infrared (Supporting Information Figures S7 and S8). These results indicate that other plasmonic substrates can also be designed to resonantly enhance the rate of energy transfer in UPL (other fluorescent and excitonic systems), while keeping the other photophysical rates relatively unchanged.

In conclusion, we found the plasmon-enhanced resonant energy transfer, likely due to strong Coulomb coupling, on easily fabricated gold pyramid pattern is enhanced at least 6 times. The quenching is also increased ∼14 times on flat metal, which points to the need for careful coupling of plasmon modes with the desired photophysical processes. These findings can benefit not only the use of UPL for renewable energy and biological applications, but can also have important implications for improving other fluorescence and excitonic systems like organic and other excitonic solar cells.

Methods. *Synthesis of Doped-Lanthanide Nanocrystals.* The codoped β-NaYF$_4$:17%Yb^{3+}/3%Er^{3+} nanocrystals were prepared by a thermal decomposition synthesis method.[13] In a typical synthesis, 90 mg Y$_2$O$_3$, 33.3 mg Yb$_2$O$_3$, and 5.7 mg Er$_2$O$_3$ were dissolved in 2 mL CH$_3$COOH. The lanthanide acetate product was then dissolved in 6 mL of oleic acid. The lanthanide mixture was held at 100 °C under a vacuum for 60 min on a Schlenk line to remove oxygen and water. A fluoride-containing solution was prepared by dissolving 82.0 mg CH$_3$COONa and 83.5 mg NaF in 2 mL of oleic acid and 10 mL of 1-octadecene. The fluoride mixture was kept at 100 °C under a vacuum for 30 min, and then purged with nitrogen. The solution was then heated under nitrogen to 320 °C within 10−15 min and maintained at this temperature. The lanthanide solution was then injected into the fluoride solution quickly (within 1 min). The homogeneous, single-phase reaction mixture was maintained at 320 °C for 30 min under nitrogen and then allowed to cool to room temperature. The nanoparticles were precipitated by the addition of ∼100 mL of acetone and were isolated by centrifugation at 5000 rpm. The samples were then washed with acetone at least three times. The final products were suspended in toluene for TEM characterization and further experiments. Figure 2a shows the TEM image of 29 nm β-NaYF$_4$:17%Yb^{3+}/3%Er^{3+} nanoparticles.

Fabrication of Nanopatterned Plasmonic Structures. We used simple chemical etching techniques to pattern the silicon substrate. When the surface of a [100]-oriented silicon wafer is exposed to a solution of KOH, anisotropic etching can lead to gold pyramidal divets.[24] We formed such patterns by coating a wafer with gold, selectively exposing the wafer with photolithography (with 2 μm periodicity circular pattern), and immersing the substrate in KOH. The divets were then coated with ∼250 nm of gold film by thermal evaporation, which was removed with epoxy to produce gold pyramid arrays (Figure 2b). The gold pyramids were smooth, highly reproducible, and exhibited sharp tips with radii of curvature as small as 10 nm[20,24] (Figure 2b). The evaporated gold film has a rough surface after deposition, but the device uses the opposite interface, which is smooth.

Confocal or Depth-Resolved Imaging. The confocal or depth-resolved imaging is performed by excitation with a 980 nm femtosecond pulse from a tunable (680−1080 nm) Ti:sapphire oscillator (140 fs, 80 MHz, Chameleon Ultra-II, Coherent) and by epi-detection with various interference filters used to separate the fluorescent light from the excitation laser beam.[31] This nonlinear optical process of two-photon absorption of β-NaYF$_4$:17%Yb^{3+}/3%Er^{3+} nanoparticles attains better resolution simultaneously with the two-photon excitation fluorescence microscopy imaging, which was obtained for red and green emissions separately by using filters. An average excitation power of 16 mW was used to obtain the confocal image shown herein. In the meantime, the photoluminescence

spectra were collected by an Ocean Optics USB4000 spectrometer.

ASSOCIATED CONTENT

Ⓢ Supporting Information

Temperature estimate, decay time analysis, two-photon analysis, detailed model of the upconversion process, detailed analysis of Purcell enhancement, quenching, and energy transfer enhancement, additional plasmonic substrates like bullseye and linear gratings, and analysis of their quenching and energy transfer enhancement. This material is available free of charge via the Internet at http://pubs.acs.org.

AUTHOR INFORMATION

Corresponding Author

*E-mail: pnagpal@colorado.edu.

Author Contributions

P.N. conceived the idea and designed the experiments. Q.C.S and P.N. synthesized the nanocrystals, fabricated the plasmonic substrates, characterized the morphology, conducted steady state and time resolved PL, and developed the theoretical model. H.M. and Q.C.S. conducted the spectrally resolved confocal measurements. J.C.R. made the templates using optical lithography and metal deposition. V.S. conducted the AFM characterization. P.N. and Q.C.S. wrote the manuscript, with input from all authors. All authors commented on the manuscript.

Notes

The authors declare no competing financial interest.

ACKNOWLEDGMENTS

REFERENCES

(1) Martí, A.; Luque, A. *Next Generation Photovoltaics: High Efficiency through Full Spectrum Utilization*; Taylor & Francis: London, 2003.

(2) Green, M. A. *Third Generation Photovoltaics: Advanced Solar Energy Conversion*, 2nd ed.; Springer: New York, 2005.

(3) Shockley, W.; Queisser, H. J. *J. Appl. Phys.* **1961**, *32*, 510−519.

(4) Shalav, A.; Richards, B. S.; Trupke, T.; Kramer, K. W.; Gudel, H. U. *Appl. Phys. Lett.* **2005**, *86*, 013505.

(5) van der Ende, B. M.; Aarts, L.; Meijerink, A. *Phys. Chem. Chem. Phys.* **2009**, *11*, 11081−11095.

(6) Vogel, A.; Venugopalan, V. *Chem. Rev.* **2003**, *103*, 577−644.

(7) Nyk, M.; Kumar, R.; Ohulchanskyy, T. Y.; Bergey, E. J.; Prasad, P. N. *Nano Lett.* **2008**, *8*, 3834−3838.

(8) Wang, F.; Liu, X. *Chem. Soc. Rev.* **2009**, *38*, 976−989.

(9) Wang, Y.-F.; Liu, G.-Y.; Sun, L.-D.; Xiao, J.-W.; Zhou, J.-C.; Yan, C.-H. *ACS Nano* **2013**, *7*, 7200−7206.

(10) Auzel, F. *Chem. Rev.* **2004**, *104*, 139−173.

(11) Haase, M.; Schaefer. *Angew. Chem., Int. Ed.* **2011**, *50*, 5808−5829.

(12) Wang, F.; Han, Y.; Lim, C. S.; Lu, Y.; Wang, J.; Xu, J.; Chen, H.; Zhang, C.; Hong, M.; Liu, X. *Nature* **2010**, *463*, 1061−1065.

(13) Lin, C.; Berry, M. T.; Anderson, R.; Smith, S.; May, P. S. *Chem. Mater.* **2009**, *21*, 3406−3413.

(14) Shan, J.; Uddi, M.; Yao, N.; Ju, Y. *Adv. Funct. Mater.* **2010**, *20*, 3530−3537.

(15) Zhao, J.; Lu, Z.; Yin, Y.; McRae, C.; Piper, J. A.; Dawes, J. M.; Jin, D.; Goldys, E. M. *Nanoscale* **2013**, *5*, 944−952.

(16) Xie, X.; Gao, N.; Deng, R.; Sun, Q.; Xu, Q.-H.; Liu, X. *J. Am. Chem. Soc.* **2013**, *135*, 12608−12611.

(17) Zhao, J.; Jin, D.; Schartner, E. P.; Lu, Y.; Liu, Y.; Zvyagin, A. V.; Zhang, L.; Dawes, J. M.; Xi, P.; Piper, J. A.; Goldys, E. M.; Monro, T. M. *Nat. Nanotechnol.* **2013**, *8*, 729−734.

(18) Ebbesen, T. W.; Lezec, H. J.; Ghaemi, H. F.; Thio, T.; Wolff, P. A. *Nature* **1998**, *391*, 667−669.

(19) Schietinger, S.; Aichele, T.; Wang, H.-Q.; Nann, T.; Benson, O. *Nano Lett.* **2010**, *10*, 134−138.

(20) Lindquist, N. C.; Nagpal, P.; Lesuffleur, A.; Norris, D. J.; Oh, S.-H. *Nano Lett.* **2010**, *10*, 1369−1373.

(21) Atwater, H. A. *Sci. Am.* **2007**, *296*, 56−63.

(22) Polman, A. *Science* **2008**, *322*, 868−869.

(23) Schuller, J. A.; Barnard, E. S.; Cai, W.; Jun, Y. C.; White, J. S.; Brongersma, M. L. *Nat. Mater.* **2010**, *9*, 193−204.

(24) Nagpal, P.; Lindquist, N. C.; Oh, S.-H.; Norris, D. J. *Science* **2009**, *325*, 594−597.

(25) Halas, N. J.; Lal, S.; Chang, W.-S.; Link, S.; Nordlander, P. *Chem. Rev.* **2011**, *111*, 3913−3961.

(26) Durach, M.; Rusina, A.; Klimov, V. I.; Stockman, M. I. *New J. Phys.* **2008**, *10*, 105011.

(27) Lakowicz, J. R. *Anal. Biochem.* **2001**, *298*, 1−24.

(28) Cao, B. S.; He, Y. Y.; Zhang, L.; Dong, B. J. *Luminescence* **2013**, *135*, 128−132.

(29) Strohhofer, C.; Polman, A. *Opt. Mater.* **2003**, *21*, 705−712.

(30) Nikolic, M. G.; Jovanovic, D. J.; Dramicanin, M. D. *Appl. Opt.* **2013**, *52*, 1716−1724.

(31) Lee, T.; Trivedi, R. P.; Smalyukh, I. I. *Opt. Lett.* **2010**, *35*, 3447−3449.